Enhanced generation of a second-harmonic wave in a composite of metamaterial and microwave plasma with various permittivities

Akinori Iwai,[1] Yoshihiro Nakamura,[1] and Osamu Sakai[1,2]

[1]*Electronic Science and Engineering, Kyoto University, Kyoto-daigaku Katsura, Nishikyo-ku, Kyoto 615-8510, Japan*

[2]*Electronic Systems Engineering, The University of Shiga Prefecture, 2500 Hassakacho, Hikone, Shiga 522-8533, Japan*

(Received 4 February 2015; published 23 September 2015)

The generation of a second-harmonic wave, which is one typical nonlinear feature, is enhanced in a composite of plasma and metamaterial. When we generate plasma by an injection of microwaves, whose frequencies are fundamental, we observe intensified second-harmonic waves in the cases of negative-refractive-index states in which both metamaterial permeability and plasma permittivity are negative for the fundamental waves. We performed the measurements at multiple levels of microwave input power up to 300 W to regulate permittivity in the negative polarity for the fundamental wave and in the transient region, including the positive-zero-negative values, for the second-harmonic wave. We clarified that the observed enhancement results from high electron density in negative-permittivity plasma, the propagating fundamental frequency wave not being attenuated in the negative-refractive-index state, and partial phase matching between the fundamental and second-harmonic waves.

DOI: 10.1103/PhysRevE.92.033105 PACS number(s): 52.25.Mq, 52.35.Mw, 52.80.Pi

I. INTRODUCTION

Second-harmonic wave generation has attracted much attention in nonlinear optics since the 1960s, when laser technology was established and enabled us to obtain highly intense electromagnetic wave sources [1]. The generation of harmonic radiation is derived from the quiver motion of electrons [2]. This generation occurs not only at a high frequency range but also at a low frequency, or the microwave range. The electric response of general homogeneous materials is linearly proportional to electric field amplitude, and this property can be shown as electric permittivity ε. In this linear case, ε is a real and constant value. However, high power wave incidence into materials in a nonlinear process induces some specific reactions, one of which is harmonic wave generation. In this nonlinear case, ε has the following expression in the Taylor series: $\varepsilon = \varepsilon_0(A_1 + A_2E + A_3E^2 + \cdots)$ [3], where ε_0 is the permittivity in a vacuum, E is the electric field intensity, and A_n is the coefficient of the $(n-1)$th-order component. Crystals with this nature have been called nonlinear crystals, which many experiments have addressed [3], but the crystals are in solid configuration with fixed electric parameters. In contrast, plasma, which is nonlinear and an experimental target for harmonic generation instead of crystals, has a reconfigurable shape and variable permittivity. For such views, a number of reports have reviewed harmonic generation in plasma with positive permittivity [4–9] and other nonlinear features with hysteresis [10,11].

Plasma permittivity depends on one of the plasma parameters, electron density n_e, which is mainly enhanced by the field power of E. However, if n_e exceeds the threshold value, which is referred to as the cutoff density, ε becomes a negative value and wave propagation into plasma is forbidden; the refractive index $N = \sqrt{\varepsilon_r\mu_r}$ [12] and plasma can only control ε_r, where ε_r is relative permittivity and μ_r is relative magnetic permeability. Therefore, μ_r must be negative for efficient interaction between negative-ε plasma and a propagating electromagnetic wave when we focus on cases of overdense plasma or negative-ε effects.

Since the 1990s, metamaterials, which are artificial dielectrics composed of metal components and play another important role in this study, have been focused on in general physics because they have special electric properties that natural materials cannot realize [13]. The resonance of individual metal patterns induces abnormal reactions to electromagnetic waves, and second-harmonic generation from metamaterials has been reported, including asymmetric circuits with elements like diodes [14–16] and conventional metamaterial patterns with magnetic force [17]. Double split ring resonators (DSRRs), which Pendry *et al.* experimentally and theoretically proposed [18], have negative magnetic permeability μ. The properties of both negative μ and nonlinearity are significant in our study.

Another typical artificial periodic structure concept is a photonic crystal, which has an extraordinary response to electromagnetic waves [19]. In this case, the replacement of dielectrics and metals with plasmas gives the photonic crystal dynamic controllability [20–22]. Our group experimentally realized plasma photonic crystals with microplasmas [23,24].

In our next study, we proposed plasma metamaterials to gain dynamic properties [25]. We clarified the ε of plasma metamaterials with a bifurcation feature in numerical simulation using an analytical model [26] and experimented on the generation of high density plasma [27,28] and the nonlinearity of plasma metamaterials [29]. In our previous report [29], we referred to second-harmonic generation from plasma metamaterials, although that report failed to show observations in various conditions and comparable results that are required to confirm the causal relationship between second-harmonic generation and the nonlinearity of plasma metamaterials.

Until this research, there have been very few studies on second-harmonic generation in negative-ε plasmas at an electron plasma frequency higher than fundamental wave frequencies. In this report, we demonstrate enhanced second-harmonic generation with the details of parameter dependencies and investigate the effects of the following three factors: high electron density, negative N at the frequency

of fundamental waves, and phase matching. High electron density, which leads to overdense plasma, may enhance second-harmonic generation. Negative ε with positive μ prevents the fundamental wave from propagating, but its propagation is possible in a negative-refractive-index state in which both ε and μ are negative. The phase matching condition is suitable for detection and potential applications of second-harmonic waves.

II. EXPERIMENTS

A. Experimental setup

To observe second-harmonic generation, we made a plasma-metamaterial composite; DSRRs were embedded by microwave plasma. The experimental setup is shown in Fig. 1. The rectangular waveguide (WR-430), in which microwaves from 1.7 to 2.6 GHz can propagate as the dominant mode [30], was installed in a vacuum chamber. This chamber, which was pumped to 10^{-4} Pa in advance, was filled with Ar gas at 100 Pa. The wave source systems were composed of a signal generator (Hewlett Packard, 8664A), an amplifier (Kyoto-Micro-Densi, MA-02400C), and a function generator for wave modulation (NF Corp., CDF-1906). A 2.45-GHz microwave modulated in a pulse with a duty ratio of 0.5% was launched from this system through the waveguide into the plasma generation space with DSRRs. The 2.45-GHz microwave has two essential roles: one is the energy source for microwave plasma generation, and the other is the fundamental wave component for second-harmonic generation. The geometric figure and the overview are illustrated in Fig. 1. Our DSRRs were fabricated in a wet etching process using thin Cu films on glass-epoxy substrates, and the Cu side was laminated by a Kapton layer with $\varepsilon_r \sim 3$. We measured μ_r of the DSRRs by a vector network analyzer (Anritsu, MA2028B) with the parameter retrieval method [31] and the Thru-Reflect-Line method [32].

The details of the derived μ_r are shown in our previous paper [29] and $\mu_r = -2.6 - 0.3j$ at 2.45 GHz while $\mu_r \sim 1$ at a higher frequency range than 3 GHz (including 4.9 GHz, the second-harmonic frequency). In comparison with a model equation of the Lorentz type, $\mu(\omega) = \mu_0[1 + F\omega^2/(\omega_0^2 - j\gamma\omega - \omega^2)]$, where ω is the angular frequency and μ_0 is the magnetic permeability in a vacuum, the estimated values are larger by a factor of ~3 than the prediction $(-0.85 - 0.09j)$ when we set typical parameters like oscillator length F of 0.22 and damping coefficient γ of $2\pi \times 14$ MHz with resonance frequency ω_0 of $2\pi \times 2.3$ GHz [33]. However, the negative-μ region is very similar (2.3–2.5 GHz), and its estimation with a negative refractive index in the results in the following section remains valid.

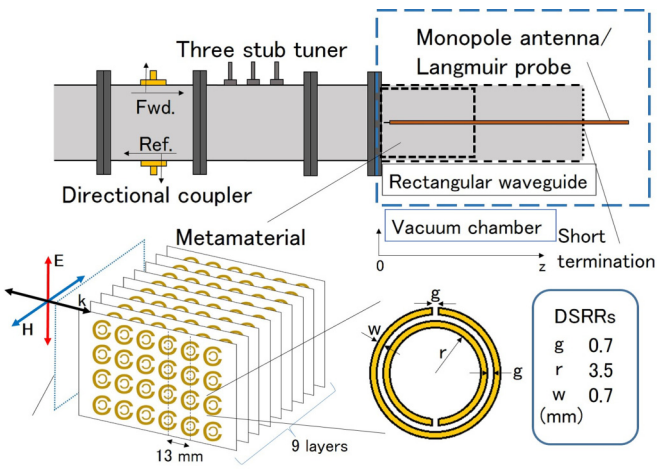

FIG. 1. (Color online) Experimental setup for microwave plasma generation in negative-μ_r space. The shape of the DSRRs was designed to fit the inner scale of the vacant waveguide.

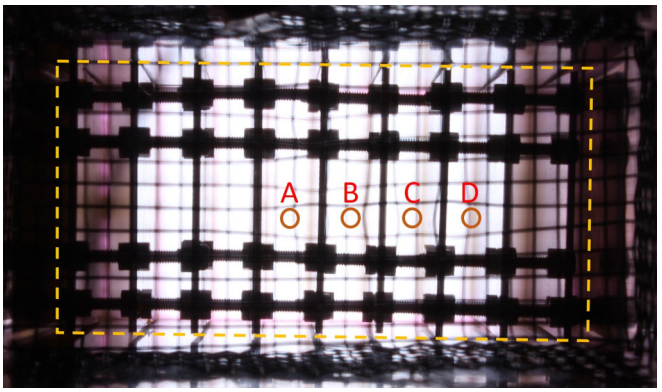

FIG. 2. (Color online) Plasma emission and DSRRs with detective position (circles). Broken lines indicate the inner frame line of the waveguide.

Second-harmonic waves (4.9-GHz) and fundamental (2.45-GHz) signals were measured by a monopole antenna that was connected to a spectrum analyzer (Aaronia Spectran, HF-60100 V4 X) by an impedance matched cable. The antenna was made from a 2.1-mm-outside-diameter and a 1-mm-diameter center core coaxial cable, whose 3-mm-length end was bare. We set this antenna 5 mm from the end of waveguide ($z = 5$ mm in Fig. 1), and the positions in the cross section of the waveguide are illustrated in Fig. 2. We replaced the antenna with the Langmuir probe when we monitored n_e. This setup closely resembles our previous work [28,29].

The absolute values of n_e, which are measured by Langmuir probes [34], may include errors by a factor of ~2 in comparison with those measured by the other methods using microwave and optical instruments that provide more accurate values [35]. The validity of the absolute-value estimation of n_e making the refractive index zero might be doubtful in the following sections because of possible errors in the measurement by the probe method, but the relative values and the data trends are invariant.

B. Experimental principle

In the case of Ar, the elastic scattering cross section for momentum transfer produces a Ramsauer minimum at about 0.1 eV [36]. Microwaves excite electrons with electron temperature $T \sim 4$ eV [29] in this experiment, and the Ramsauer effect is negligible in this high energy range; the cross section σ becomes large. The elastic collision frequency ν is expressed as $\nu = \sigma n_N v_{th}$ [37]. Here n_N is the neutral particle density and v_{th} is the thermal velocity, $v_{th} = \sqrt{8k_BT/\pi m_e}$, which is the net electron velocity in plasma as a function of T, where k_B is the Boltzmann constant and m_e is the electron mass. When

the electron energy is 4 eV in Ar gas at 100 Pa, the elastic collision frequency ν becomes 1.7 GHz [36]. We assume that the incident electric field has oscillation component $e^{j(kz-\omega t)}$, where k is the wave number, z is the location in the propagation direction, and t is time. ε_r of this experimental condition has the following form, as shown in the Appendix:

$$\varepsilon_r = 1 - \frac{1}{\omega^2\left(1+j\frac{\nu}{\omega}\right)}\frac{e^2 n_e}{m_e\varepsilon_0} - \frac{c^2}{\mu_r\omega^2}\left(\frac{\pi}{a}\right)^2, \qquad (1)$$

where e is an electron charge, n_e is the electron density, ε_0 is the permittivity in the vacuum, c is the light velocity in the vacuum, μ_r is the relative permeability of the DSRRs, and a is the wider inside dimension of the waveguide. In this paper, $\omega/2\pi = 2.45$ GHz and $\nu/\omega \sim 0.1$, which indicates that ν hardly influenced ε. As a result, we assume collisionless plasma in this condition and ε_r is approximately

$$\varepsilon_r = 1 - \frac{1}{\omega^2}\frac{e^2 n_e}{m_e\varepsilon_0} - \frac{c^2}{\mu_r\omega^2}\left(\frac{\pi}{a}\right)^2. \qquad (2)$$

C. Experimental results

To control ε_r and N in plasma that becomes 2.45-GHz wave media and 4.9-GHz signal generation, we varied the input microwave power up to 300 W in the DSRR space. From Eq. (2) and the measurement results of n_e [Fig. 3(a)], we get Figs. 3(b), 3(c), and 4.

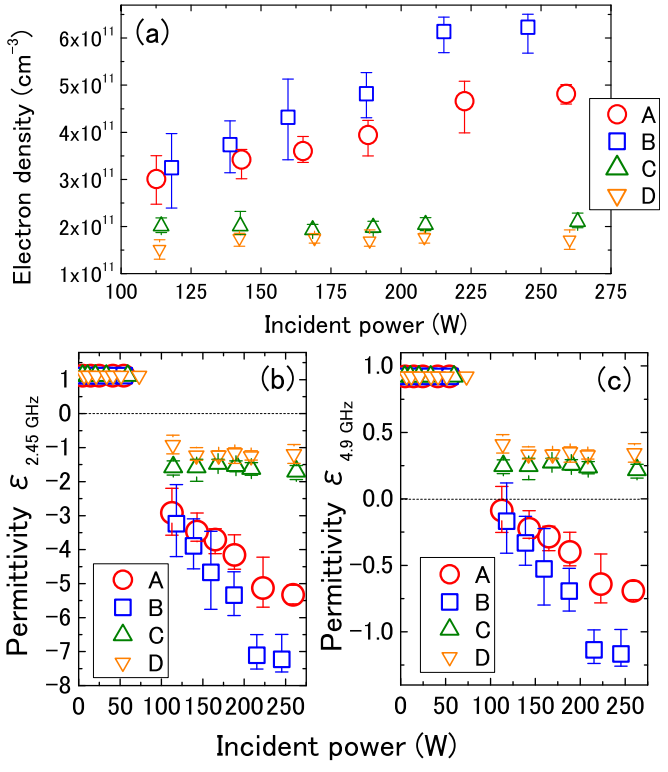

FIG. 3. (Color online) (a) n_e as a function of incident microwave power at several positions in Fig. 2 with DSRRs. (b), (c) Different behaviors of ε_r over positions based on n_e profiles. Broken lines express $\varepsilon_r = 0$. (b) At 2.45 GHz, the imaginary part has constant value -0.01j. (c) At 4.9 GHz, ε_r is a real number because $\mu_r = 1$ and the third term in Eq. (2) is a real number.

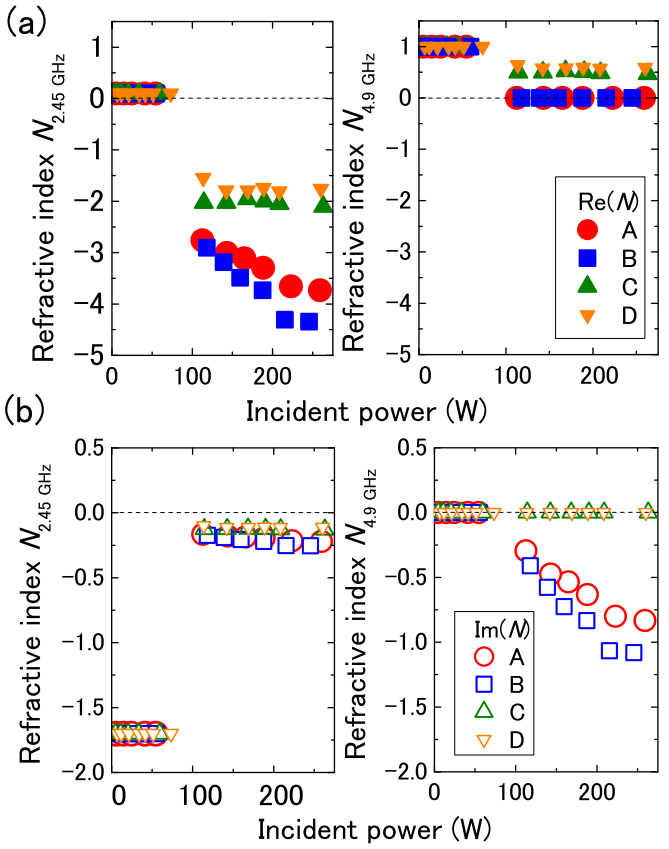

FIG. 4. (Color online) Refractive index N derived from ε_r and μ_r as a function of incident power with DSRRs. Real and imaginary parts of N are expressed as Re(N) and Im(N). Real components affect wave propagation, and imaginary ones significantly influence wave attenuation. Broken lines express $N = 0$: (a) real part and (b) imaginary part.

Figures 3(b) and 3(c) show the differences of local ε over the spatial positions. ε mainly depends on n_e beyond the threshold power, and the second term of Eq. (2) becomes the dominant component. ε at 2.45 GHz becomes negative at every position with plasma, which indicates the overdense plasma that occupies the waveguide. Although ε is negative, n_e increases as the increment of input power at central positions A and B. This is supported by the synthesized effects of negative-ε plasma and negative-μ DSRRs. The input microwave that is lower than the lowest ignition power induces very simple ε, which is decided by Eq. (2) where its second term is negligible. In the free space, the microwave has a TEM mode and propagates in the dispersionless media with $\varepsilon_r = 1$. On the other hand, DSRRs and a rectangular waveguide, which are dispersive media, affect wave propagation in this experimental condition. Therefore, ε_r without plasma is a function of ω and μ_r and does not equal 1 exactly. Moreover, there is a small imaginary part: -0.01j.

In Fig. 4, we define the local refractive index N as a product of the square roots of ε_r (local permittivity) and μ_r (macroscopic permeability). Plasma generation reverses the relationship between the real and imaginary parts of N at 2.45 GHz. The double negative parameters make N a real and negative value after plasma ignition. In contrast, without plasma, the square root of μ_r, $\sqrt{\mu_r} = 0.1 - 1.6$j,

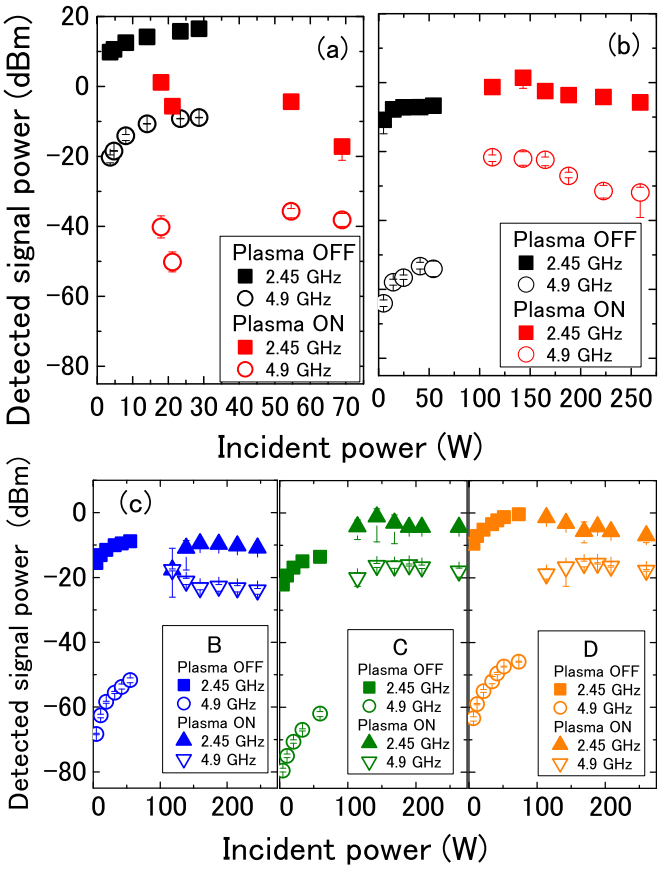

FIG. 5. (Color online) (a), (b) Detected signals of 2.45 and 4.9 GHz when antenna was at position A in Fig. 2: (a) without DSRRs and (b) with DSRRs. (c) Detected signals when antenna is at other positions, B, C, and D, in Fig. 2.

mainly determines N because $\varepsilon_r \sim 1$, and N becomes a purely imaginary value and forbids fundamental waves from propagating. N at 4.9 GHz has a different profile from the one for 2.45 GHz. After plasma ignition, negative-ε plasma makes N imaginary at positions A and B, and positive-ε plasma makes N real at positions C and D. In contrast, the case without plasma shows a very similar value to the free space. This difference is based on the following facts. In Fig. 3(c), ε at 4.9 GHz has an opposite sign at positions A and B and positions C and D because n_e is not beyond the cutoff electron density for the 4.9-GHz wave at positions C and D.

For various parameter sets of ε_r and N shown in Figs. 3 and 4, we measured the wave signals of the fundamental and second-harmonic components. Figures 5(a) and 5(b) show the different behaviors of the 2.45- and 4.9-GHz signals as a function of the incident microwave power at position A (Fig. 2) with or without DSRRs.

With DSRRs, plasma ignition clearly enhances the 4.9-GHz component and only slightly changes the 2.45-GHz signals (or provides a slight *increase*) in Fig. 5(b); without DSRRs, both frequency signals decrease by plasma generation in Fig. 5(a). The difference of the 4.9-GHz signal intensity in Figs. 5(a) and 5(b) is explained as follows. DSRRs cancel the plasma effect (imaginary N by overdense n_e), which forbids wave propagation. After plasma ignition, we observe no decrement of the 2.45-GHz signals in Fig. 5(b), but the others decrease from 55 to 70 W in Fig. 5(a) because of negative-μ DSRRs. However, the fundamental wave energy is dissipated in the higher-density-plasma generation and in the more intense second-harmonic wave generation in a nonlinear process, which leads to a similar intense detection on 2.45 GHz in spite of the existence of DSRRs [red squares in Figs. 5(a) and 5(b)]. From 20 to 55 W in Fig. 5(a), the incident power increments boost the 4.9-GHz signal but not the 2.45-GHz signal, which indicates that the interaction between the plasma without DSRRs and the electric field just induces a slight second-harmonic wave generation. Second-harmonic generation in pure plasma is reviewed in the Appendix. However, plasma with DSRRs can give more intense second-harmonic wave signals.

Without plasma (Fig. 4), $\varepsilon_r \sim 1$, $N = \sqrt{\mu_r} = 0.1 - 1.6j$, and the attenuation factor, which is the imaginary part of N, becomes the dominant component of N. The 2.45-GHz microwave evanescently enters the negative-μ_r space, and weaker signals are detected before plasma generation, contrary to the case without DSRRs [black squares in Figs. 5(a) and 5(b)]. The detected 4.9-GHz signals have certain values before the generation of plasma [black circular outlined plots in Figs. 5(a) and 5(b)], and we refer to this in the description of Fig. 6.

When we changed the in-plane positional condition of the waveguide [Figs. 5(b) and 5(c)], both frequency signals had similar profiles as the functions of the incident power; plasma ignition boosts the 4.9-GHz signal power and immediately triggers second-harmonic wave generation. Plasma with DSRRs maintains 2.45 GHz around -10 dBm when the input power exceeds 100 W, indicating that negative-ε plasma and negative-μ DSRRs are synthesized in the 2.45-GHz range not only at the center of the waveguide but also near the edge. Even though the 4.9-GHz signals start from about -20 dBm at every position when the incident power is beyond the plasma-ignition power, they have two contractive profiles: at positions A and B and at positions C and D. In the former case, the incident power increment attenuates the detected signal power, but the latter profile hardly has any variation in the incident power. These results can be explained by N in Fig. 4 and suggest that the second-harmonic wave is attenuated only at positions A and B, and the 4.9-GHz wave becomes the evanescent one at positions A and B and the propagating one at positions C and D.

Figure 6(a) has two axes with the same scale size. If the 2.45-GHz signals have linear relationships to the 4.9-GHz signals, straight lines can be drawn with slope angle 45°. However, the plots in the case without plasma are on a line whose angle is about 60°, which is clearly beyond 45°. This indicates that, besides plasma and DSRRs, these experimental systems include a certain amount of nonlinearity for incident electric fields, and the evaluation of second-harmonic wave generation from the net plasma effects requires careful treatment.

In cases with DSRRs after plasma ignition, open symbols exist on the upper side from this line [in chain-outlined area in Fig. 6(a)]. Along the line, plots are for cases without plasma. These facts indicate that DSRRs enhance the absolute intensity of second-harmonic waves, although the detected

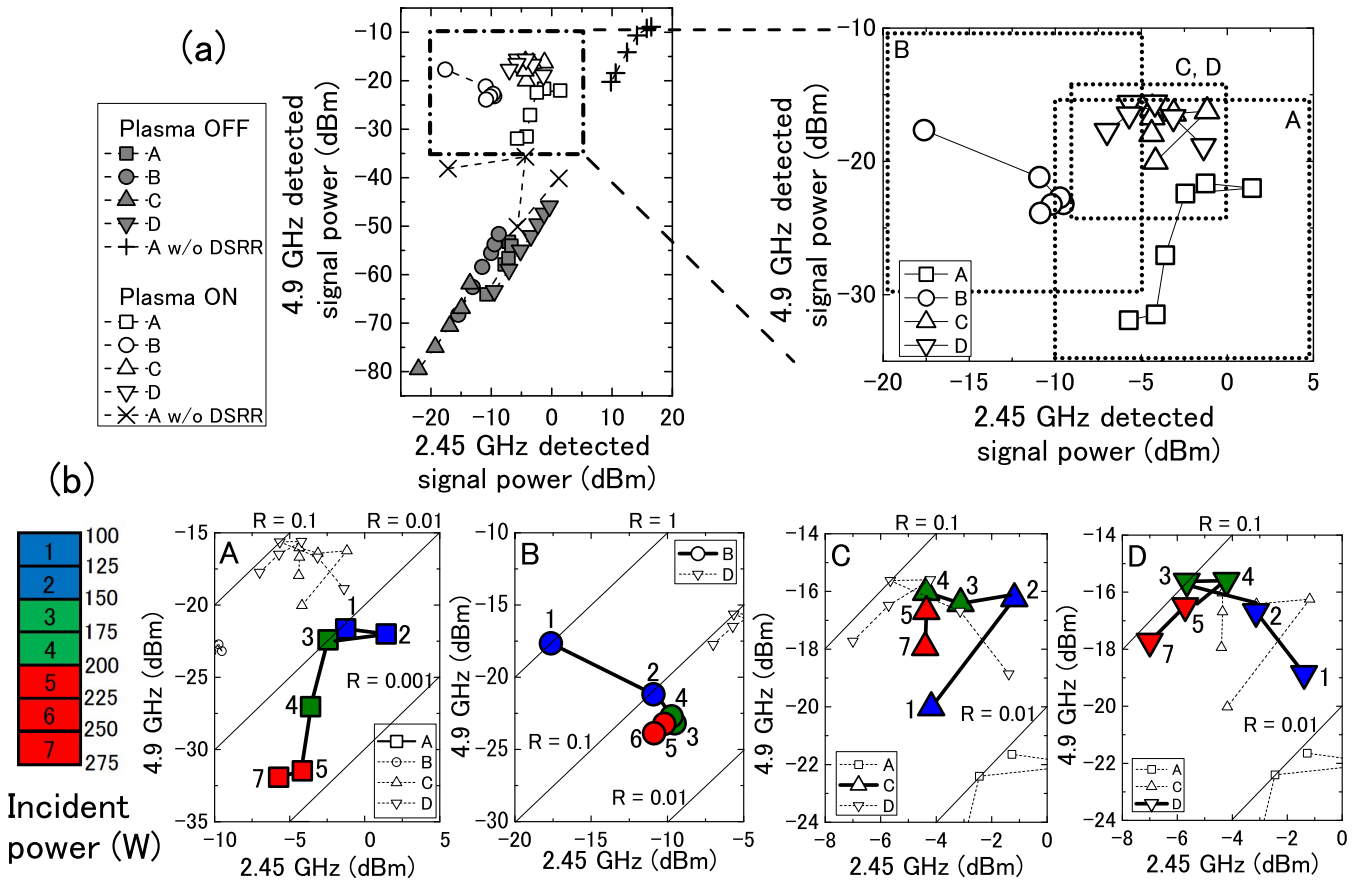

FIG. 6. (Color online) Change of 2.45- and 4.9-GHz signals from input power. Squares, circles, triangles, and upside-down triangles indicate measurement results with DSRRs at positions A, B, C, and D, respectively. For DSRRs, gray-shaded symbols (input power is under 100 W) indicate results without plasma generated beyond 100 W. (b) Enlarged figure of chain-outlined area in (a). Diagonals are lines on which the ratio R is constant between 2.45- and 4.9-GHz detected signal power $R = 10^{(P_{4.9\ \mathrm{GHz}} - P_{2.45\ \mathrm{GHz}})/10}$. $P_{2.45\ \mathrm{GHz}}$ and $P_{4.9\ \mathrm{GHz}}$ are 2.45- and 4.9-GHz detected signal power for identical input power. Numbers from 1 to 7 indicate levels of incident power after plasma ignition.

fundamental frequency signals still have similar values. In contrast, without DSRRs, cross plots are found on the straight line, and the first two ×-mark plots are on the same line after plasma generation. Such a tendency implies that the original nonlinearity of plasma does not induce second-harmonic wave generation when the incident power is slightly above the lowest ignition power for the generation of plasma. Even if the input microwave power increases, the second-harmonic wave power hits a comparatively low ceiling because of the overdense plasma.

We cannot simultaneously observe the fundamental and second-harmonic wave signals because of this experimental system and repeat discharge shots to acquire both signals. But the ratio between 2.45- and 4.9-GHz R [Fig. 6(b)] becomes a reliable measure to check how efficiently second-harmonic wave generation occurred since it is generated by the interaction between a fundamental wave and plasma at each spot.

As shown in Fig. 6(b), the presence of DSRRs puts the plots in a higher R area. The results at positions C and D have very similar profiles and keep the signals around −18 dBm and $R \sim 0.03$. The data points at positions A and B have large changes including similar and opposite features. The similar feature is the decrement of the 4.9-GHz intensity and R when the input power increases because N is imaginary at 4.9 GHz. The opposite one is that the blue circles (input power is 118 W at position B) are in a special high R area, which is caused by a unique phase condition. In the next section, we survey this event from the aspect of phase matching, which is based on conventional nonlinear optics.

III. DISCUSSION

Fundamental waves induce a double-frequency-oscillating dipole that leads to second-harmonic wave radiation in plasma. Inherent plasma dispersion creates a phase difference between nonlinear-dipole oscillation and second-harmonic waves and induces destructive interference [Fig. 7(a)]. Conversely, efficient frequency conversion requires a reduction of this difference, and this condition is called "phase matching" [38]. From Eq. (A15) in the Appendix, the dispersion relationship has the following form:

$$k = \frac{\omega}{c} N. \tag{3}$$

To satisfy the phase matching in the second-harmonic wave generation process, it is required that $2k_{\mathrm{f}} = k_{\mathrm{s}}$, where k_{f} is

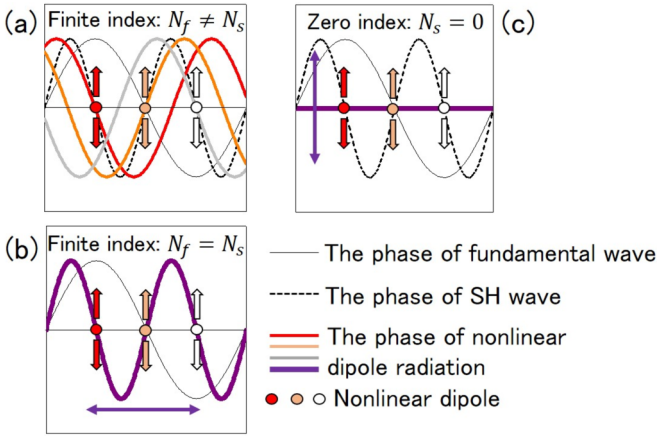

FIG. 7. (Color online) Phase condition on each index relation. Bold purple lines indicate overlap of red, orange, and light gray lines. (a) Second-harmonic wave radiation from each dipole passively obeys dispersion. (b) Each radiation wave has the same phase and a coherent interference is derived. (c) There is no phase because of group or plasma oscillation.

the wave number of the fundamental wave and k_s is that of the second-harmonic wave. Substituting this relationship into Eq. (3) results in $N_f = N_s$ [Fig. 7(b)].

A general nonlinear crystal has constant N for each polarization and requires a simple phase matching condition. However, our experimental plasma with scale limitation has spatial N variation, which requires that each positional phase matching be fulfilled. Phase mismatch, which is defined as $\Delta k = k_s - 2k_f$, is the essential parameter of a nonlinear process because $2\pi/\Delta k$ (the coherence length) is the period of the amplitude oscillation of the generated second-harmonic waves [3]. Based on Eq. (3),

$$\Delta k = \frac{\omega_f}{c}(N_s - N_f), \tag{4}$$

where $\omega_f/2\pi = 2.45$ GHz. Here we do not have to consider the imaginary part of N because it is associated only with the spatial attenuation of the wave amplitude. Figure 4 shows $N_s - N_f \gtrsim 3$ and indicates

$$\frac{2\pi}{\Delta k} \lesssim 20 \text{ mm}. \tag{5}$$

Our experimental setup generates plasma with a z directional length of about 20 mm [28], and the coherence length is less than the plasma spatial length. This experiment includes the spatial power variation of second-harmonic wave generation in plasma space by phase mismatch and has no positions that satisfy phase matching; however, it does have the following unique feature.

When the input power is ∼120 W, the electron density of positions A and B is very close to the 4.9-GHz cutoff density (2.8×10^{11} cm^{-3}) and N at 4.9 GHz is near 0. It is possible that the plasma metamaterials work in a zero-index condition [Fig. 7(c)]. The second-harmonic wave has no phase mismatch, and this condition can induce constructive interference. In fact, the real part of N at 4.9 GHz is 0 at positions A and B, and the increment of the imaginary part induces attenuation. For example, if $N = -0.8$j, the skin depth is about 12 mm, which is smaller than the plasma size of this experiment (∼20 mm), and the attenuation from imaginary N is not negligible; therefore, an efficient process requires that both the real and imaginary parts of N are 0.

As mentioned above, in these experimental results, the phase-mismatch-free condition can occur under the following three conditions: (1) at positions A and B, (2) when the input power is around 120 W, which is the lowest power after plasma ignition, and (3) with DSRRs.

In Figs. 5(a), 5(b), and 6, the ratio between the 4.9- and 2.45-GHz signal intensities without DSRRs exceeds that with DSRRs at the highest incident power. However, this fact does not indicate efficient second-harmonic generation in plasma without DSRRs because the 2.45-GHz wave was attenuated in overdense plasma and the denominator of the ratio decreases solely as the input power is raised.

In our experimental plasma, n_e depends on spatial uniformity sensitively [39] and we could not simultaneously measure the signal intensity and n_e in our current experimental setup. Perhaps there was a slight spatial difference between the monopole antenna and the Langmuir probe in our experiment at position A. In other words, the zero-index condition sensitively depends on the spatial variation; however, Fig. 5(b) shows a tendency for results at position A that satisfy the zero-index condition when input power is ∼120 W because a large decrement of the 4.9-GHz signal occurs as the input power is increased beyond 120 W and the phase of the 4.9-GHz signal is far from the phase-mismatch-free point.

One may be skeptical about the collaboration of continuum plasma and the discrete structures of the DSRR array. However, this enhancement of second-harmonic signals is well understood by the effective refractive index for ε by the plasma and for μ by the DSRRs array. In other words, the state of the negative-ε plasma and the space under the cutoff condition of the microwave waveguide make a similar macroscopic condition for propagating an electromagnetic wave [40]. We conclude that we successfully synthesized μ by a DSRR array established under the metamaterial concept and ε from positive to negative values mainly controlled by n_e in plasma.

IV. CONCLUSION

We experimentally verified the enhanced generation of second-harmonic waves with negative-ε plasma and μ by metamaterial (DSRR array). Based on the inherent nonlinearity in a general plasma, the efficient generation of second-harmonic waves was induced by the three features: high n_e, propagation of fundamental waves in the negative-refractive-index state, and partial phase matching. In particular, ε is closely controlled by varying n_e, and the properties shown in the experimental data are well understood by the complex values of the refractive index.

ACKNOWLEDGMENTS

This work was partly supported by a Grant-in-Aid for Scientific Research from the Japanese Ministry of Education,

Culture, Sports, Science and Technology and by Casio Science Promotion Foundation.

APPENDIX A: PLASMA PERMITTIVITY IN WAVEGUIDE

The following are Maxwell's equations:

$$\nabla \times \mathbf{H} = \mathbf{J} + \frac{\partial \mathbf{D}}{\partial t}, \tag{A1}$$

$$\nabla \times \mathbf{E} = -\frac{\partial \mathbf{B}}{\partial t}, \tag{A2}$$

$$\nabla \cdot \mathbf{B} = 0, \tag{A3}$$

$$\nabla \cdot \mathbf{D} = \rho_{\mathrm{e}}. \tag{A4}$$

Here $\mathbf{H}$ is the magnetic field vector, $\mathbf{J}$ is the current density vector, $\mathbf{D}$ is the electric flux density vector, $\mathbf{E}$ is the electric field vector, $\mathbf{B}$ is the magnetic flux density vector, and ρ_{e} is the charge density in the unit volume. We assume that plasma is an isotropic medium and that μ_{r} only depends on DSRRs, which gives the following formations:

$$\mathbf{D} = \varepsilon_0 \mathbf{E}, \tag{A5}$$

$$\mathbf{B} = \mu_{\mathrm{r}} \mu_0 \mathbf{H}, \tag{A6}$$

where μ_0 is the permeability in a vacuum. The dominant mode of the incident microwave electric field is the TE_{10} mode in our experimental waveguide, which gives the following formation [41]:

$$\mathbf{E} = \begin{pmatrix} 0 \\ A \sin\left(\frac{\pi x}{a}\right) e^{\mathrm{j}(kz-\omega t)} \\ 0 \end{pmatrix}, \tag{A7}$$

where z is the wave propagation direction and the wide and narrow sides of the waveguide are along the x and y axes. According to Eqs. (A1) and (A2),

$$\nabla \times (\nabla \times \mathbf{E}) = -\mu_{\mathrm{r}} \mu_0 \frac{\partial \mathbf{J}}{\partial t} - \mu_{\mathrm{r}} \mu_0 \varepsilon_0 \frac{\partial^2 \mathbf{E}}{\partial t^2}. \tag{A8}$$

$\mathbf{E}$ has only a y axis component E_{y}, which is a function of x, z, and t. As a result,

$$\nabla \times (\nabla \times \mathbf{E}) = \begin{pmatrix} 0 \\ -\frac{\partial^2 E_{\mathrm{y}}}{\partial x^2} - \frac{\partial^2 E_{\mathrm{y}}}{\partial z^2} \\ 0 \end{pmatrix}. \tag{A9}$$

Ohm's law and the conductivity of plasma, σ, give

$$\mathbf{J} = \sigma \mathbf{E}. \tag{A10}$$

Finally we have the following expression from Eqs. (A8)–(A10):

$$\left(\frac{\pi}{a}\right)^2 + k^2 = \mathrm{j}\mu_{\mathrm{r}} \mu_0 \omega \sigma + \mu_{\mathrm{r}} \mu_0 \varepsilon_0 \omega^2. \tag{A11}$$

We can also get the plasma's momentum balance equation by considering the electric field and the elastic collision:

$$m_{\mathrm{e}} \frac{d\mathbf{v}}{dt} = -e\mathbf{E} - m_{\mathrm{e}} \nu \mathbf{v}. \tag{A12}$$

Here $\mathbf{v}$ is an electron velocity vector. The electron oscillation by the electric field and current density $\mathbf{J} = -en_{\mathrm{e}}\mathbf{v}$ make the following expression for σ:

$$\sigma = \frac{e^2 n_{\mathrm{e}}}{m_{\mathrm{e}}(\nu - \mathrm{j}\omega)}. \tag{A13}$$

Substituting Eq. (A13) for Eq. (A11) induces the following dispersion relation of this condition:

$$k^2 = \frac{\omega^2}{c^2} \mu_{\mathrm{r}} \left\{ 1 - \frac{1}{\omega^2 \left(1 + \mathrm{j}\frac{\nu}{\omega}\right)} \frac{e^2 n_{\mathrm{e}}}{m_{\mathrm{e}} \varepsilon_0} - \frac{c^2}{\mu_{\mathrm{r}} \omega^2} \left(\frac{\pi}{a}\right)^2 \right\}. \tag{A14}$$

In the general dielectric case, the dispersion relation has this form:

$$k^2 = \frac{\omega^2}{c^2} \mu_{\mathrm{r}} \varepsilon_{\mathrm{r}}. \tag{A15}$$

Consequently, ε_{r} of this experimental condition is

$$\varepsilon_{\mathrm{r}} = 1 - \frac{1}{\omega^2 \left(1 + \mathrm{j}\frac{\nu}{\omega}\right)} \frac{e^2 n_{\mathrm{e}}}{m_{\mathrm{e}} \varepsilon_0} - \frac{c^2}{\mu_{\mathrm{r}} \omega^2} \left(\frac{\pi}{a}\right)^2. \tag{A16}$$

APPENDIX B: GENERATION OF SECOND-HARMONIC FIELD IN PLASMA

Even though the following discussion is based on previous work [42], we treat n_{e} with spatial variation as $n_{\mathrm{e}}(\mathbf{x})$ in this paper. Here $\mathbf{x}$ is a spatial position. The plasma's momentum balance equation, which includes nonlinear terms in the collisionless case, is

$$m_{\mathrm{e}} \frac{\partial \mathbf{v}}{\partial t} + m_{\mathrm{e}} (\mathbf{v} \cdot \nabla)\mathbf{v} = -e\mathbf{E} - e(\mathbf{v} \times \mathbf{B}). \tag{B1}$$

In Eq. (B1), $\mathbf{v}$, $\mathbf{E}$, and $\mathbf{B}$ are represented by a Fourier series in the following form:

$$\mathbf{v} = \sum_{\mathrm{i}} \mathbf{v}_{\mathrm{i}} e^{-\mathrm{j}(\mathrm{i}\omega)t}, \tag{B2}$$

$$\mathbf{E} = \sum_{\mathrm{i}} \mathbf{E}_{\mathrm{i}} e^{-\mathrm{j}(\mathrm{i}\omega)t}, \tag{B3}$$

$$\mathbf{B} = \sum_{\mathrm{i}} \mathbf{B}_{\mathrm{i}} e^{-\mathrm{j}(\mathrm{i}\omega)t}. \tag{B4}$$

From Eqs. (B1) and (A2), the first-order components of $\mathbf{v}$ and $\mathbf{B}$ are expressed as follows:

$$\mathbf{v}_1 = \frac{e}{\mathrm{j}\omega m_{\mathrm{e}}} \mathbf{E}_1, \tag{B5}$$

$$\mathbf{B}_1 = \frac{1}{\mathrm{j}\omega} \nabla \times \mathbf{E}_1. \tag{B6}$$

Inserting these equations into Eq. (B1) produces a second-order equation:

$$-2\mathrm{j}\omega m_{\mathrm{e}} \mathbf{v}_2 + e\mathbf{E}_2 = \frac{e^2}{2\omega^2 m_{\mathrm{e}}} \nabla(\mathbf{E}_1 \cdot \mathbf{E}_1) \equiv \mathbf{F}_{\mathrm{pf}}. \tag{B7}$$

The center part of Eq. (B7) is called the ponderomotive force, which we defined as $\mathbf{F}_{\mathrm{pf}}$. If n_{e} has quiver variation n' by the electromagnetic waves, the electron flux continuity and Gauss's law equations have the following expressions:

$$\frac{\partial n'}{\partial t} + \nabla(n_{\mathrm{e}} \mathbf{v}_2) = 0, \tag{B8}$$

$$-en' = \varepsilon_0 \nabla \cdot \mathbf{E}_2. \tag{B9}$$

Substituting Eqs. (B7) and (B9) for Eq. (B8) produces the following form:

$$(\nabla n_e) e\mathbf{E}_2 = \left(\frac{e^2 n_e}{\varepsilon_0} - 4\omega^2 m_e\right) n' + \nabla(n_e \mathbf{F}_{pf}). \quad \text{(B10)}$$

If we assume that $n' \sim 10^{12}$ m^{-3}, the ratio between $|\mathbf{E}_2|$ ($\sim$1 V/m for $|\nabla n_e| \sim 10^{21}$ m^{-4}) and $|\mathbf{E}_1|$ ($\sim$100 V/m) resembles the experimental results in Fig. 5(a).

[1] D. L. Mills, *Nonlinear Optics Basic Concept Second, Enlarged Edition* (Springer, New York, 1998).
[2] P. Gibbon, IEEE J. Quantum Electron. **33**, 1915 (1997).
[3] R. W. Boyd, *Nonlinear Optics, Third Edition* (Elsevier, London, 2008).
[4] E. Takahashi, M. Mori, N. Yugami, Y. Nishida, and K. Kondo, Phys. Rev. E **65**, 016402 (2001).
[5] R. B. Piejak and V. A. Godyak, Appl. Phys. Lett. **76**, 2188 (2000).
[6] K. P. Singh, D. N. Gupta, S. Yadav, and V. K. Tripathi, Phys. Plasmas **12**, 013101 (2005).
[7] P. Jha, R. K. Mishra, G. Raj, and K. Upadhyay, Phys. Plasmas **14**, 053107 (2007).
[8] H. R. Askari and Z. Azish, Optik (Munich, Ger.) **122**, 1159 (2011).
[9] Y. Yasaka, H. Takeno, M. Sakka, O. Sakai, R. Itatani, T. Fujimoto, H. Suemitsu, K. Takahata, M. Fukao, S. Tanaka, and Y. Terumichi, Plasma Phys. Controlled Fusion **35**, 379 (1993).
[10] O. Sakai, Y. Yasaka, and R. Itatani, Phys. Rev. Lett. **70**, 4071 (1993).
[11] O. Sakai and Y. Yasaka, Phys. Plasmas **2**, 3249 (1995).
[12] V. G. Veselago, Sov. Phys. Usp. **10**, 509 (1968).
[13] A. Lipson, S. G. Lipson, and H. Lipson, *Optical Physics, 4th Edition* (Cambridge University Press, New York, 2011).
[14] Z. Wang, Y. Luo, L. Peng, J. Huangfu, T. Jiang, D. Wang, H. Chen, and L. Ran, Appl. Phys. Lett. **94**, 134102 (2009).
[15] T. Kanazawa, Y. Tamayama, T. Nakanishi, and M. Kitano, Appl. Phys. Lett. **99**, 024101 (2011).
[16] T. Nakanishi, Y. Tamayama, and M. Kitano, Appl. Phys. Lett. **100**, 044103 (2012).
[17] M. W. Klein, C. Enkrich, M. Wegener, and S. Linden, Science **313**, 502 (2006).
[18] J. B. Pendry, A. J. Holden, D. J. Robbins, and W. J. Stewart, IEEE Trans. Microwave Theory Tech. **47**, 2075 (1999).
[19] M. Skorobogatiy and J. Yang, *Fundamentals of Photonic Crystal Guiding* (Cambridge University Press, New York, 2009).
[20] H. Hojo and A. Mase, J. Plasma Fusion Res. **80**, 89 (2004).
[21] B. Guo, Phys. Plasmas **16**, 043508 (2009).
[22] B. Guo and M. Q. Xie, Optik (Munich, Ger.) **125**, 2137 (2014).
[23] T. Naito, O. Sakai, and K. Tachibana, Appl. Phys. Express **1**, 066003 (2008).
[24] O. Sakai, T. Sakaguchi, and K. Tachibana, Appl. Phys. Lett. **87**, 241505 (2005).
[25] O. Sakai and K. Tachibana, Plasma Source Sci. Technol. **21**, 013001 (2012).
[26] O. Sakai, J. Appl. Phys. **109**, 084914 (2011).
[27] O. Sakai, S. Iio, and Y. Nakamura, Plasma Fusion Res. **8**, 1406167 (2013).
[28] Y. Nakamura and O. Sakai, Jpn. J. Appl. Phys. **53**, 03DB04 (2014).
[29] Y. Nakamura, A. Iwai, and O. Sakai, Plasma Source Sci. Technol. **23**, 064009 (2014).
[30] S. F. Adam, *Microwave Theory and Applications* (Prentice-Hall, Englewood Cliffs, NJ, 1969).
[31] D. R. Smith, D. C. Vier, T. Koschny, and C. M. Soukoulis, Phys. Rev. E **71**, 036617 (2005).
[32] D. M. Pozar, *Microwave Engineering* (John-Wiley & Sons, Hoboken, 2011).
[33] A. Rose, D. Huang, and D. R. Smith, Phys. Rev. Lett. **107**, 063902 (2011).
[34] O. Sakai, Y. Kishimoto, and K. Tachibana, J. Phys. D **38**, 431 (2005).
[35] K. Urabe, H. Muneoka, S. Stauss, and K. Terashima, Plasma Source Sci. Technol. **23**, 064007 (2014).
[36] L. S. Frost and A. V. Phelps, Phys. Rev. **136**, A1538 (1964).
[37] R. J. Goldston and P. H. Rutherford, *Introduction to Plasma Physics* (Taylor & Francis, New York, 1995).
[38] H. Schowski, K. O'Brien, Z. Wong, A. Salandrino, X. Yin, and X. Zhang, Science **342**, 1223 (2013).
[39] A. Iwai, Y. Nakamura, A. Bambina, and O. Sakai, Appl. Phys. Express **8**, 056201 (2015).
[40] H. Sugai, I. Ghanashev, and M. Nagatsu, Plasma Sources Sci. Technol. **7**, 192 (1998).
[41] A. D. Oliver, *Microwave and Optical Transmission* (Wiley, West Sussex, 1992).
[42] S. K. Sinha and A. C. Sinha, Phys. Plasmas **3**, 59 (1996).